

STATISTICAL MECHANICS OF COLLISIONLESS ORBITS. IV. DISTRIBUTION OF ANGULAR MOMENTUM

LILIYA L. R. WILLIAMS<sup>1</sup>, JENS HJORTH<sup>2</sup>, AND RADOSŁAW WOJTAK<sup>2</sup>

Received 2013 August 12; accepted 2014 January 8

ABSTRACT

It has been shown in previous work that DARKexp, which is a theoretically derived, maximum entropy, one shape parameter model for isotropic collisionless systems, provides very good fits to simulated and observed dark-matter halos. Specifically, it fits the energy distribution,  $N(E)$ , and the density profiles, including the central cusp. Here, we extend DARKexp  $N(E)$  to include the distribution in angular momentum,  $L^2$ , for spherically symmetric systems. First, we argue, based on theoretical, semi-analytical, and simulation results, that while dark-matter halos are relaxed in energy, they are not nearly as relaxed in angular momentum, which precludes using maximum entropy to uniquely derive  $N(E, L^2)$ . Instead, we require that when integrating  $N(E, L^2)$  over squared angular momenta one retrieves the DARKexp  $N(E)$ . Starting with a general expression for  $N(E, L^2)$  we show how the distribution of particles in  $L^2$  is related to the shape of the velocity distribution function, VDF, and velocity anisotropy profile,  $\beta(r)$ . We then demonstrate that astrophysically realistic halos, as judged by the VDF shape and  $\beta(r)$ , must have linear or convex distributions in  $L^2$ , for each separate energy bin. The distribution in energy of the most bound particles must be nearly flat, and become more tilted in favor of radial orbits for less bound particles. These results are consistent with numerical simulations and represent an important step towards deriving the full distribution function for spherically symmetric dark-matter halos.

*Subject headings:* dark matter — galaxies: halos

1. INTRODUCTION

The full dynamical description of relaxed dark-matter halos is of fundamental importance for our basic understanding as well as for more practical applications in galaxy formation and evolution, and cosmology. N-body simulations have converged on the properties of dark-matter halos (Navarro et al. 2004; Stadel et al. 2009; Navarro et al. 2010), though some uncertainty may still remain arising from finite resolution effects.

A lot of work has been devoted to attempts to explain the density and velocity structure of relaxed halos by examining the dynamical processes at work, like mass accretion rate, conservation of radial action, radial orbit instability, etc. (e.g., Le Delliou & Henriksen 2003; Williams et al. 2004; Lu et al. 2006; Salvador-Solé et al. 2007; Ascasibar et al. 2007; Dalal et al. 2010). Though such phenomenological arguments are valuable and bring insight to the problem, they do not arise directly from fundamental physics. Because the properties of virialized dark matter halos appear universal, and are only weakly dependent on initial conditions, like cosmological model, local density, etc., it is reasonable to assume that the structure of halos is governed by physics more fundamental than that described by phenomenology.

Motivated by the possibility of a first principles solution, several groups have attempted a statistical mechanics approach. To our knowledge, the first attempts were made by Ogorodnikov (1957) and Lynden-Bell (1967), with somewhat limited success (see Hjorth & Williams

2010, hereafter Paper I, for a discussion). Several other works have appeared since (Stiavelli & Bertin 1987; Hjorth & Madsen 1991; Spergel & Hernquist 1992; Chavanis 1998; Levin et al. 2008; Lapi & Cavaliere 2009; Pontzen & Governato 2013). Some of these rely on arbitrary assumptions, while others require many parameters to fit halos adequately.

Our statistical mechanics approach (Paper I) differs from the previous ones in that we work in a different state space, which we argue is more appropriate for collisionless systems, and uses an accurate description of low occupation numbers, which appears to be important for self-gravitating systems (see also Madsen 1996). In Paper I we derived the differential mass, or energy distribution,  $dM/dE = N(E)$  for collisionless material under the assumption that the final steady-state configuration represents the most likely state, and therefore can be obtained as a maximum entropy state. Our model is called DARKexp, and its energy distribution is  $N(\epsilon) = \exp(\phi_0 - \epsilon) - 1$ , where  $\epsilon = \tilde{\beta}E$  is the dimensionless energy,  $\tilde{\beta}$  is the inverse thermodynamic temperature ( $\tilde{\beta} < 0$ ), and  $\phi_0 = \tilde{\beta}\Phi_0$  is the dimensionless central potential.

Unlike other theoretically motivated density profiles (King 1966; Lynden-Bell 1967; Madsen 1996), DARKexp predicts central density cusps. The asymptotic, small  $r$  density slope for all central potentials,  $\phi_0$ , is  $d \ln \rho / d \ln r = -1$ , but for radii accessible to N-body simulations, the central slope varies depending on  $\phi_0$ :  $\phi_0 \lesssim 4$  systems have inner slopes shallower than  $-1$ , while  $\phi_0 \gtrsim 5$  have inner slopes between  $-1$  and  $-2$ .

DARKexp appears to be a very good descriptor of the energy distribution and density profile of dynamical systems: galaxy and galaxy cluster size dark-matter halos in

<sup>1</sup> School of Physics and Astronomy, University of Minnesota, 116 Church Street SE, Minneapolis, MN 55455, USA; llrw@astro.umn.edu

<sup>2</sup> Dark Cosmology Centre, Niels Bohr Institute, University of Copenhagen, Juliane Maries Vej 30, DK-2100 Copenhagen Ø, Denmark; jens@dark-cosmology.dk, wojtak@dark-cosmology.dk

simulations (Williams et al. 2010, hereafter Paper III), observed galaxy clusters (Beraldo e Silva et al. 2013), and even many globular clusters (Williams et al. 2012). Beraldo e Silva et al. (2013) compared a range of theoretical and phenomenological models to relaxed galaxy clusters whose profiles were estimated using strong and weak lensing. DARKexp did better than other theoretical models, and performed as well as the best empirical fitting functions.

The DARKexp model derived in Paper I has one limitation: it describes the distribution of particles in energy only, i.e.,  $N(E)$ , and implicitly assumes that the distribution in angular momentum corresponds to that of a system with an isotropic velocity ellipsoid. While velocity anisotropy (hereafter, anisotropy) affects the shape of  $N(E)$  only weakly, one still would like to know the full dynamical description of a system, including the distribution of particles in angular momentum,  $L$ . Systems considered in this work have no net rotation, so the angular momentum vector is reduced to its modulus. Dark-matter halos in simulations, and probably in the Universe are not isotropic. Therefore one needs to extend DARKexp  $N(E)$  to include  $L^2$ .

This paper is devoted to estimating  $N(E, L^2)$  from basic arguments and simple models. In Section 2 we discuss the degree of mixing in energy and angular momentum and argue that a maximum entropy approach may not be applicable to the problem in hand. Instead we propose an integral constraint on  $N(E, L^2)$ . In Section 3 we generate and characterize halos obeying this constraint and compare to simulated halos. Section 4 provides a summary and an outlook.

## 2. GENERAL CONSIDERATIONS FOR $N(E, L^2)$

### 2.1. *The lack of mixing of angular momenta*

Relaxation into equilibrium, or at least into a long-lived steady state can be driven by any dynamical process that mixes, or redistributes, particle energies and angular momenta, thereby causing them to be uncorrelated with the corresponding initial values. Dark-matter halos in simulations are nearly relaxed systems, though the degree of relaxation is still not clear. In a collisionless system, mixing in energy is achieved because the particles exchange energy with the global time-varying potential (Lynden-Bell 1967), while mixing in angular momentum is accomplished through torques which are present in any system that deviates from spherical symmetry.

We now argue that dark-matter halos are not as well relaxed in angular momentum as they are in energy. This difference in the degree of relaxation in the two parameters,  $E$  and  $L^2$ , is possible because relaxation in energy and in angular momentum can proceed relatively independently of each other, at least in some systems. One example is the Extended Secondary Infall Model (ESIM), described in Williams & Hjorth (2010, hereafter Paper II) and some earlier works (Ryden & Gunn 1987; Williams et al. 2004). ESIM systems relax through spherically symmetric collapse in which particles/orbits keep their initial  $L^2$  throughout the evolution. Even though  $L^2$  of individual particles do not change at all, the corresponding  $E$  does change significantly, and the final virialized halos are well fit with DARKexp. Therefore mixing and relaxation in  $E$  can be achieved, without

having any mixing in  $L^2$ .

Numerically simulated dark-matter halos in equilibrium are relaxed in energy as evidenced by their being well fit with DARKexp (Paper III). Figure 1 contains four individual halos and their DARKexp fits that make up the average shown in that paper. The fit at very large negative energies (i.e. for very bound particles) and intermediate energies is very good; at small negative energies (right side of each panel) most of the particles are quite far from the halo center, and so may not be in equilibrium.

Are the halos equally well relaxed in  $L^2$ ? Apparently not. Wojtak et al. (2013) show that the principal axes of cosmologically simulated halos are aligned with the *local* velocity ellipsoids, and the alignment is strongest in the innermost shells. Moreover, the principal axes are aligned with the large scale structure filaments (Libeskind et al. 2013) which implies that the angular distribution of angular momentum,  $\mathbf{L}$ , retains the memory of the formation process, down to the inner most regions. If mixing in angle were complete, as required by full relaxation, these alignments should have been erased.

Why are halos not well mixed in  $L^2$ ? We speculate that this is because in a collapsing system, radial forces, and hence changes in radial forces, tend to be larger and longer lasting than tangential ones. The former are largely responsible for mixing in  $E$ , while the latter are exclusively responsible for mixing in  $L^2$ . In other words, radial fluctuations in the gravitational potential are more dominant than tangential ones, where the latter are brought about by ellipticity, substructure and merging.

### 2.2. *Failure of maximum entropy arguments for the angular momenta*

As a consequence, this observation implies that theoretical maximum entropy approaches that assume full mixing in angle and require  $L^2$  to be part of the entropy (e.g., Pontzen & Governato 2013), likely cannot capture the properties of simulated dark-matter halos. To check that free redistribution or mixing of  $L^2$  is not taking place in collapsing systems, we considered the final state of a system assuming that it does. In other words, we apply a maximum entropy argument to  $L^2$  as well as to  $E$ . To do this we extend our derivation presented in Paper I to include angular momentum. As in that paper, a maximum entropy procedure is applied, where in addition to the total energy and total mass, a quantity relating to the total angular momentum is also held fixed. Apart from the fact that there are now three, rather than two, Lagrange multipliers, the maximization of entropy procedure is the same as the one used to derive the isotropic DARKexp. The final derived distribution has the form

$$N(E, L^2) \propto \exp(\tilde{\beta}\Phi_0 - \tilde{\beta}E - \gamma L^\xi) - 1, \quad (1)$$

which is analogous to Equation (30) of Hjorth (1994). (Note that  $\tilde{\beta}$  in the above is not to be confused with the velocity anisotropy. We denote the velocity anisotropy by  $\beta$  or  $\beta(r)$ .)

In general, there is no analytical way to derive the density profiles from Equation (1). We therefore used an iterative procedure, similar to the one used in Paper II, to obtain the corresponding density profiles. We exper-

imented with several combinations of parameters  $\gamma$  and  $\xi$  (see Appendix A for details). Some parameter combinations did not produce viable halos, i.e., did not converge. Those that did converge had velocity anisotropy profiles that were isotropic at small radii and became tangentially anisotropic at large radii. Because no dynamically produced collisionless systems is known to have such anisotropy, and because it seems unlikely that any dynamical process would lead to such a system, we conclude that systems described by Equation (1), with  $\gamma \neq 0$ , do not exist in simulations, or the real Universe.

One could argue that the choice of a power law form for  $L$  in Equation (1) is limiting, and there could be other functional forms that would produce realistic systems. While possible, we speculate that the general behaviour of solutions will be similar to that displayed by Equation (1), regardless of the what function of  $L$  is used. A more thorough investigation is needed to explore this question.

Though Equation (1) cannot be solved analytically to produce  $\rho(r)$  in general, in Appendix B we consider a special case that can be solved analytically. In this case the density profile is

$$\rho(r) = \frac{1}{4\pi} \left( -\frac{\tilde{\beta}}{\gamma\xi} \right)^{2/(\xi-2)} \left( \frac{2+\xi}{2-\xi} \right) r^{-4(\xi-1)/(\xi-2)}, \quad (2)$$

where  $\tilde{\beta} < 0$ ,  $\gamma < 0$ , and  $-2 < \xi < 0$ . Equation (2) is a power law, ranging in slope between  $\rho \propto r^{-2}$  and  $\rho \propto r^{-3}$ . These are grossly inconsistent with the profiles obtained in simulations, whose slopes are not constant, and steepen with radius from around  $-1$  to  $-3$  well within the virial radius (e.g., Navarro et al. 1997).

Because Equation (1) does not seem to produce systems with realistic density profiles and constant or increasing velocity anisotropy profiles, we conclude that the maximum entropy argument cannot be used to derive the energy and angular momentum distribution of dynamically evolved collisionless systems. The combined evidence of the arguments presented above leads us to conclude that dynamically evolved collisionless systems are not as well relaxed in angular momentum as they are in energy; in other words, the particle angular momenta  $\mathbf{L}$ , and hence their moduli  $L$  are not as freely redistributed during evolution as their energies.

### 2.3. Proposed integral form for $N(E, L^2)$

Our hypothesis that mixing in  $E$  is achieved relatively quickly and efficiently, while mixing in  $L^2$  is not, suggests that the general form for  $N(E, L^2)$  should be

$$N_{\text{DARKexp}}(E) = \int_0^{L_{\text{max}}^2(E)} N(E, L^2) dL^2. \quad (3)$$

Here  $N(E, L^2)$  is non-separable, and upon integration over all angular momenta gives DARKexp  $N(E)$ . This means that systems that have DARKexp  $N(E)$  can have a range of  $L^2$  distributions. The different types of  $L^2$  distributions can, for example, come about as a consequence of different formation scenarios, such as cosmological vs. isolated collapse.

Equation (3) is also consistent with an unrelated property of differential energy distributions in general. Differential energy distributions,  $N(E)$ , depend primarily on

the density profile, with little dependence on the velocity anisotropy. The velocity anisotropy is defined in the usual way,  $\beta(r) = 1 - [\sigma_\theta(r)/\sigma_r(r)]^2$ , where  $\sigma_\theta$  and  $\sigma_r$  are velocity dispersions in one of the tangential directions, and radial direction, respectively. Anisotropy is determined by the distribution of particles/orbits in  $L^2$ . This means that a given  $\rho(r)$ , coupled with different forms for  $\beta(r)$ , will result in nearly the same  $N(E)$ . The insensitivity of  $N(E)$  to velocity anisotropy was pointed out by Binney & Tremaine (2008) (their Section 4.4 and Figure 4.15b) using isotropic and fully radially anisotropic Jaffe models.

This lack of sensitivity of  $N(E)$  to the velocity anisotropy ensures that DARKexp density profile, derived for isotropic orbits, should also describe anisotropic cosmological N-body simulated halos, as was shown explicitly in Paper III. The recent finding by Beraldo e Silva et al. (2013) that DARKexp density profiles provide very good fits to observed galaxy clusters, whose galaxies (Biviano & Poggianti 2009; Biviano et al. 2013) and dark matter (Host et al. 2009) appear to have radial velocity anisotropy at large radii, is also consistent with the energy distribution being largely independent of anisotropy.

In Section 3 we will use Equation (3) to arrive at the full distribution of particles in  $E$  and  $L^2$ , or  $N(E, L^2)$ .

## 3. DISTRIBUTION OF $L^2$ IN HALOS

We generate as wide a range of  $N(E, L^2)$  distributions as possible, all satisfying Equation (3).  $N(E)$  is identical for all systems, and the density profiles are similar for all halos (DARKexp  $\phi_0 = 4$ ). The major difference between systems is in the velocity dependent properties, which are related to the  $L^2$  distribution. We then ask how the distribution of particles in angular momentum relates to the astrophysically relevant halo quantities, namely the velocity distribution function, VDF, and the anisotropy profile,  $\beta(r)$ . Here we will mostly deal with the radial VDF, which is a histogram of radial speeds of particles (with respect to the halo center) in a specified radial range within the halo.

In order to find a relation between  $N(E, L^2)$ , the VDF and  $\beta(r)$ , we need to quantify these properties in a succinct way, such that, for example, the entire  $\beta(r)$  profile is represented by a single value. We do this in Section 3.2. Even though all our halos are physically possible, not all are astrophysically realistic. For example, an astrophysically realistic halo cannot have large (spherically averaged)  $\beta(r)$  at small radii. We then isolate  $N(E, L^2)$  distributions that give rise to astrophysically realistic VDFs and anisotropy profiles.

### 3.1. Generating the $L^2$ distributions

The general method for generating  $N(E, L^2)$  uses Equation (3). We start with the DARKexp form for  $N(E)$ , and at each energy distribute particles in  $L^2$  according to some prescription. (Same method as used in Paper III.) We work with dimensionless energy units,  $\epsilon$ , defined in Paper I, and  $\ell^2 = L^2/L_{\text{circ}}^2$ , where  $L_{\text{circ}}(\epsilon)$  is the angular momentum for a circular orbit at that energy. We use a total of eight different prescriptions. Here is one

example:

$$N(\epsilon, \ell^2) = N_{\text{DARKexp}}(\epsilon) \left[ 1 - \frac{a}{c+1} \left( \frac{\phi_0 - \epsilon}{\phi_0} \right)^b \right]^{-1} \times \left[ 1 - a \left( \frac{\phi_0 - \epsilon}{\phi_0} \right)^b (\ell^2)^c \right]. \quad (4)$$

The first square bracket contains the normalization factor, which depends on energy, while the second square bracket contains the dependence on  $L$  and energy. This makes  $N(E, L^2)$  non-separable (as is true for all our prescriptions). Another example is

$$N(\epsilon, \ell^2) = N_{\text{DARKexp}}(\epsilon) \left[ b^{-1} c^{1/b} \left( \frac{\phi_0 - \epsilon}{\phi_0} \right)^{-a/b} \times \int_0^{t_{\text{circ}}} e^{-t} t^{1/b-1} dt \right]^{-1} e^{-t}, \quad (5)$$

$$t = c^{-1} \left( \frac{\phi_0 - \epsilon}{\phi_0} \right)^a \ell^{2b},$$

where the expression in the square brackets is the normalization factor, and is proportional to the lower incomplete gamma function, with  $t_{\text{circ}}$  being  $t$  when  $L = L_{\text{circ}}$ , or  $\ell = 1$ . Note that constants  $a$ ,  $b$ , and  $c$  in Equations (4) and (5) are not the same. Different realizations of Equations (4) and (5) use a range of values for these constants.

We used density profiles for DARKexp  $\phi_0 = 4$ ; other values of  $\phi_0$  and other types of profiles give similar results. Each  $L^2$  distribution results in a different anisotropy profile. Figure 2 shows the anisotropy profiles of all the halos used in this paper. They span a wide range of possibilities. The subset of these profiles that are similar to those in cosmological N-body  $\Lambda$ CDM simulations are shown as black curves in Figure 3. The simulations are represented here by two recent works. The blue curve is the average profile from Fig. 3b of Ludlow et al. (2011). The green curves are the average and upper and lower limits of relaxed systems taken from Lemze et al. (2012) (blue curves in their Fig. 13). Because their radius is in units of the virial radius while our systems do not have a defined virial radius, we scaled their horizontal axis to have the same velocity anisotropy value at  $r_{-2}$  as the Ludlow et al. (2011) data. This may not be the optimal scaling, but whatever scaling one adopts, it is clear that different simulations do not completely agree with each other. This is also clear from the examination of the seven  $\beta(r)$  profiles presented in Fig. 11b of Navarro et al. (2010).

In Figure 4 we show an example of one of our halos. The upper left panel shows one possible prescription for the distribution in  $(L/L_{\text{circ}})^2$  of particles binned by energy into six energy  $\epsilon$  bins. The most bound particles (black and red histograms) show nearly uniform distribution in  $L^2$ . A perfectly uniform distribution would result in an isotropic system (Williams et al. 2010). The least bound particles (magenta and blue histograms) are biased toward radial orbits, and the near circular orbits are completely absent at these energies. The upper right panel has the full  $N(E, L^2)$  distribution, shown with linear and log vertical axis. The magenta line represents circular orbits. The linear plot shows that for the least bound particles, at  $\epsilon \gtrsim 2$ , near circular orbits are absent. The lower left panel has radial (main plot) and tangential

(inset) VDF. We denote the radial VDF distribution by  $N_{ur}(u_r)$ , where  $u_r = v_r/\sigma_r$ , and  $\sigma_r$  is the radial velocity dispersion at that radius. The area under each VDF is normalized to 1,  $\int_0^\infty N_{ur}(u_r) du_r = 1$ . For all the halos we considered tangential VDFs peak at  $u_t = 0$ . This is not so for radial VDF, which sometimes show deficits of orbits at small radial speeds. In this case the third radial bin from the center (blue histogram) shows a central ‘crater’. The lower right panel shows the density profile,  $\rho(r)$  as  $\log(\rho r^2)$  (thick solid line), of DARKexp with  $\phi_0 = 4$ , and the anisotropy profile,  $\beta(r)$  (dashed line). The thin solid line is the NFW profile shown here for comparison. The horizontal axis is in units of  $r_{-2}$ , the radius where the logarithmic density slope,  $d \ln \rho(r)/d \ln r$ , is equal to  $-2$ .

### 3.2. Characterizing the $L^2$ distributions

To see how the distribution in  $L^2$  is related to the VDF shape and  $\beta(r)$ , we need to characterize all three quantities with simple parameters.

We start with the  $L^2$  distribution. For any given energy  $\epsilon$ , the distribution of particles in  $\ell^2 \equiv (L/L_{\text{circ}})^2$  is denoted by  $N_{L^2}(\ell^2)$ , which is normalized,  $\int_0^1 N_{L^2}(\ell^2) d\ell^2 = 1$ , where, by definition,  $\ell^2$  runs from 0 to 1. We define the *curvature* of the  $N_{L^2}(\ell^2)$  distribution for a given  $\epsilon$  as

$$\tilde{K}(\epsilon) = \frac{\int_0^1 [N_{L^2}(\ell^2) - N_{L^2}(\ell_m^2)] d\ell^2}{[N_{L^2}(0) - N_{L^2}(\ell_m^2)] \ell_m^2 / 2} - 1, \quad K = \left\langle \tilde{K}(\epsilon) \right\rangle_{\text{all } \epsilon} \quad (6)$$

where  $\ell_m$  is the largest  $\ell$  where  $N_{L^2}(\ell^2)$  is non-zero. In the upper left panel of Figure 4, the distributions corresponding to the most bound particles (black and red histograms) have  $\ell_m = 1$ , while the distribution corresponding to the least bound particles (blue histogram) has  $\ell_m^2 = 0.76$ , and near circular orbits are completely absent. In words, Equation (6) is an expression for the curvature of the line connecting the highest point of  $N_{L^2}(\ell^2)$ , i.e., at  $\ell = 0$  and the lowest point,  $N_{L^2}(\ell^2 = \ell_m^2)$ .  $K(\epsilon)$  is 0 for straight-line distributions, negative for convex (sagging)  $N_{L^2}(\ell^2)$  distributions, and positive for concave (upward ‘bulging’)  $N_{L^2}(\ell^2)$  distributions. The curvatures of all six histograms in this figure are positive,  $K > 0$ .

We define two more quantities for  $N_{L^2}(\ell^2)$ . The *average vertical extent* of the  $N_{L^2}(\ell^2)$  histograms,

$$\bar{\Delta} = \left\langle N_{L^2}(\ell=0) - N_{L^2}(\ell=1) \right\rangle_{\text{all } \epsilon}, \quad (7)$$

and the *vertical rms dispersion* between the  $N_{L^2}(\ell^2)$  histograms, which we call  $\Delta_{\text{rms}}$ . It quantifies how spread out the histograms at various energies are. If the distributions in  $N_{L^2}(\ell^2)$  coincide at all energies, then  $\Delta_{\text{rms}} = 0$ . For the halo shown in Figure 4,  $\bar{\Delta} = 1.26$  and  $\Delta_{\text{rms}} = 0.26$ .

Next, we quantify the shape of the VDF. Because our ultimate goal is to separate plausible halos from implausible ones we are especially interested in the crater, which we consider unphysical. (VDFs of N-body simulations are either flat-topped or peaked at small speeds, see Kuhlen et al. 2010; Hansen & Sparre 2012). Let  $u_{rm}$  be the radial speed where  $N_{ur}(u_r)$  is the largest. For VDFs

that peak at  $u_r = 0$ ,  $u_{rm} = 0$ , but for those with a crater,  $u_{rm} > 0$ . The *fractional area of the radial VDF crater* is

$$\Upsilon = \int_0^{u_{rm}} [N_{ur}(u_r = u_{rm}) - N_{ur}(u_r)] du_r. \quad (8)$$

In the case of Figure 4 the blue VDF in the lower left panel has  $\Upsilon = 0.058$ .

Finally, we quantify the shape of the anisotropy profile,  $\beta(r)$ . We consider  $\beta(r)$  to be realistic if it is either increasing or staying constant with radius, and nearly zero (i.e., isotropic) at very small radii. (We remove and do not consider systems with anisotropy profiles that are monotonically falling at all radii.) With that in mind, we define  $\beta_0$  to be the value at  $\log(r/r_{-2}) = -1.5$  and  $\beta_{\min}$  to be the minimum value attained in the radial range between  $\log(r/r_{-2}) = -1.5$  and 0.  $\beta_{\min}$  is not always the same as  $\beta_0$  because some anisotropy profiles have minima between  $\log(r/r_{-2}) = -1.5$  and 0, and then increase at larger  $r$ . We quantify the  $\beta$  profile with  $B = \beta_0 + \beta_{\min}$ . This definition is somewhat arbitrary, and other variants of  $B$  can be adopted. The anisotropy profile shown in the lower right panel of Figure 4 has  $B = 0.02$ .

### 3.3. Relating the $L^2$ distributions to the halo velocity properties

Having characterized  $N_{L^2}$ , the VDF, and  $\beta(r)$  with simple parameters, we can now ask how the distribution of angular momentum,  $N_{L^2}$ , is reflected in the halos' VDF and  $\beta(r)$ . In Figure 5 we plot  $\bar{\Delta}$  vs.  $\Delta_{\text{rms}}$ , both of which are determined from  $N_{L^2}$ . Red triangle points represent halos with VDF craters,  $\Upsilon > 0$ . Magenta squares represent halos with  $B > 0.1$ . Both of these types of systems are unrealistic. It is immediately obvious from the plot that these two types of systems tend to inhabit different parts of the plot, roughly separated by a straight diagonal line. Most of the systems close to the line are astrophysically realistic (blue filled dots). However, there are some systems with VDF craters that are mixed in (red triangles among blue dots).

Figure 6 shows only a portion of the Figure 5 diagram; it cuts out systems with large  $\bar{\Delta}$  and  $\Delta_{\text{rms}}$ , which have large anisotropies, close to 1, at large radii. In Figure 6 we show that VDF crater systems ( $\Upsilon > 0$ ) can be identified and hence eliminated by using another property of the  $N_{L^2}(\ell^2)$  distributions, namely the curvature  $K$ , defined by Equation (6). Points marked with red crosses have  $K > 0$ . There is a very close correspondence between red triangles and red crosses. In other words,  $N_{L^2}(\ell^2)$  distributions that are concave ( $K > 0$ ) almost always have VDF craters ( $\Upsilon > 0$ ), and systems that have VDF craters are almost always concave.

Figure 6 shows that convex  $K < 0$  systems restricted to lie in the box around the diagonal line have realistic VDF and  $\beta(r)$  profiles. This selection uses  $\bar{\Delta}$ ,  $\Delta_{\text{rms}}$  and  $K$ , i.e., it is based solely on the shape of  $N_{L^2}(\ell^2)$ . In Figure 6 we have therefore accomplished our goal of isolating  $N_{L^2}$  shapes that gives rise to realistic systems.

Figure 7 shows three examples of realistic halos (blue dots inside the diagonal rectangle in Figure 6). Note that all three are isotropic at small radii, which is a consequence of  $N_{L^2}$  being nearly flat at very large negative energies (black and red histograms in the left panels).

For less negative energies the  $N_{L^2}$  distributions favor low angular momentum orbits, but in such a way that  $N_{L^2}$  is convex. The larger the  $\bar{\Delta}$  the larger the velocity anisotropy at large  $r$ . These anisotropy profiles are not dissimilar to those seen in cosmological simulations, represented here by two recent works, Ludlow et al. (2011); Lemze et al. (2012); see Section 3.1 for details.

Unfortunately, Figure 6 does not provide a completely clean separation because the shapes of VDF and anisotropy profiles depend on the detailed properties of the  $L^2$  distribution, which cannot be fully captured with simple global parameters. In Figure 8 we show three more systems inside the diagonal rectangle of Figure 6. The top set of panels shows a system that is correctly eliminated by our criteria as unrealistic: its  $N_{L^2}$  is concave, and it has VDF craters. The middle set of panels is a system for which our selection criteria fail by a small amount: the system's  $B = 0.106$ , which is just outside our limit of 0.1. It is represented by a magenta square in the upper portion of the diagonal rectangle. The bottom set of panels contains a system where our criteria fail, but in the opposite sense: they eliminate a realistic system because it has a slightly concave  $N_{L^2}$  shape,  $K > 0$  (one of the blue dots with a red cross through it).

The bottom panels of Figures 7 and 8 were generated using the Equation (4) prescription for distributing orbits in  $L^2$ , while the top panels of Figure 7 and the middle panels of Figure 8 were generated using Equation (5). Equation (5) (with constant  $c \gtrsim 0.2$ ) is probably the best among the ones we tried in terms of generating systems that tend to lie mostly in the diagonal rectangle of realistic halos. Note that its dependence on  $L^2$  is of exponential form  $e^{-t(L^2)}$ , similar to the exponential dependence on energy in the DARKexp  $N(E)$ .

The systems in Figure 7 can be compared qualitatively with typical halos from N-body simulations, shown in Figure 9. This is based on a sample of 36 cluster-size relaxed halos extracted from a  $z = 0$  snapshot of an N-body simulation of a standard  $\Lambda$ CDM cosmological model (for details of the simulation and the halo catalog, see Wojtak et al. 2008). This halo sample has already been used for calculating the six-dimensional distribution function as a function of energy and angular momentum, and testing its phenomenological model with radially changing anisotropy (Wojtak et al. 2008). Each halo contains from  $5 \times 10^5$  to  $5 \times 10^6$  particles inside its virial sphere defined in terms of the mean overdensity,  $\langle \rho \rangle / \rho_{\text{crit}} \approx 100$ , where  $\rho_{\text{crit}}$  is the present critical density. The energy distribution of these halos was also used in Paper III.

We conclude that realistic systems are characterized by two main properties of their  $N_{L^2}$ : (1)  $N_{L^2}$  shapes are straight or convex ( $K \leq 0$ ), and (2) the dispersion in  $N_{L^2}$  for different energies ( $\Delta_{\text{rms}}$ ) is proportional to the average vertical extent of the  $N_{L^2}$  distributions ( $\bar{\Delta}$ ), i.e., the systems lie inside the diagonal rectangular box of Figure 6.

## 4. SUMMARY AND CONCLUSIONS

While DARKexp  $N(E)$  was arrived at through statistical mechanics maximum entropy analysis, the extension to  $N(E, L^2)$  considered in this paper is not. Instead, our starting premise was Equation (3), which is the integral

equation for the isotropic DARKexp, and is based on the assumption that obtaining the distribution of particles in  $E$  is different from that in  $L^2$ . The two different treatments—maximum entropy for  $E$  and a phenomenological approach for  $L^2$ —are appropriate because, as we argue in Section 2, self-gravitating collapsing systems are free to redistribute their particles in  $E$ , but not in  $L^2$ . Because the redistribution of angular momentum is not unrestricted, not all portions of the  $L^2$  space are equally accessible, making maximum entropy arguments inappropriate.

By investigating the properties of a large number of halos all consistent with Equation (3) we conclude that astrophysically realistic halos must have  $N([L/L_{\text{circ}}]^2)$  distributions (for each energy separately) that are linear or somewhat convex in  $(L/L_{\text{circ}})^2$ . Also, the  $N([L/L_{\text{circ}}]^2)$  distribution for most bound particles (largest negative energies) must be uniform, and become more tilted in favor of radial orbits for less bound parti-

cles. We give two examples of a prescription for  $N(E, L^2)$  that generates realistic systems: Equations (4) and (5). The approximate constant ranges for Equation (4) are:  $1 < a < 2$ ,  $0.5 < b < 1.5$ , and  $0.5 < c < 1.5$ , and for Equation (5):  $1 < a < 3$ ,  $0 < b < 1.5$ , and  $c > 0.2$ .

What can give rise to such  $N([L/L_{\text{circ}}]^2)$  distributions? We argued above that because the particles are not well mixed in  $L^2$ , the distribution in  $L^2$  probably depends on the details of the initial conditions and dynamics of halo collapse, like radial orbit, and other instabilities, and is possibly somewhat different for isolated vs. cosmological collapses. The advantage of our approach is that because we considered all astrophysically realistic systems, it encompasses both of these, as well as other possible cases. Our next step is to use the form of  $N([L/L_{\text{circ}}]^2)$  obtained here to generate the distribution function  $f(E, L^2)$ , which can be compared to  $f(E, L^2)$  measured from N-body simulations (e.g., Wojtak et al. 2008).

## APPENDIX

### APPENDIX A

Suppose some  $L$ -distribution is conserved as a part of a statistical mechanical approach, which also conserves total mass and energy. The distribution in energy and angular momentum that corresponds to the most likely state is given by

$$N(E, L^2) \propto \exp(\tilde{\beta}\Phi_0 - \tilde{\beta}E - \gamma L^\xi) - 1. \quad (\text{A1})$$

This is analogous to Equation (30) of Hjorth (1994). We show below that the density profiles that correspond to Equation (A1) are not the same as for DARKexp, and that the velocity anisotropy profiles become more tangential with increasing radius. Thus these systems are very different from those seen in numerical simulations.

We note that not all  $(\gamma, \xi)$  parameter combinations produce density profiles. Systems with  $\gamma > 0$  or  $\xi < 0$  did not converge, and neither did systems with  $\gamma \ll -10$  or  $\xi \gg 1$ . In Figure 10 we show two systems that did converge. Their parameters are  $\gamma = -1$ ,  $\xi = 0.5$ ,  $\phi_0 = 6$  (top panels), and  $\gamma = -5$ ,  $\xi = 0.2$ ,  $\phi_0 = 6$ . Other systems have similar general characteristics.

### APPENDIX B

Here we consider a special sub-class of systems described by Equation (1), which produce analytical solutions.

The  $N(E, L^2)$  distribution can be represented in the  $E$  vs.  $L^2$  plane. For every  $E$  there is a maximum  $L = L_{\text{circ}} = L_c$  that corresponds to the circular orbit of that energy. The set of these  $L_c$  forms an ‘upper’ envelope in the  $E$  vs.  $L^2$  plane. In a general case the density of particles along that envelope will vary as a function of  $E$ . Let us suppose that there is a sub-class of systems where the density is constant. Then Equation (A1) reduces to  $N(E_c, L_c^2) = \text{const.}$  on that envelope. Equivalently,  $\tilde{\beta}\Phi_0 - \tilde{\beta}E_c - \gamma L_c^\xi = \text{const.}$  Differentiating, we get

$$\frac{dE_c}{dL_c^\xi} = -\frac{\gamma}{\tilde{\beta}} = \text{const.}, \quad (\text{B1})$$

because  $\gamma$  and  $\tilde{\beta}$  are constants for a given system. The left hand side of Equation (B1) can be expressed differently, as it refers to circular orbits. Circular speed  $v_c$  is given by  $v_c^2 = rd\Phi/dr$ , and the corresponding energy is  $E_c = \frac{1}{2}v_c^2 + \Phi$ . Using these we get  $E_c = \frac{1}{2}r\Phi' + \Phi$ , and  $L_c^2 = r^3\Phi'$ , where primes denote differentiation with respect to radius. Next, we can obtain expressions for  $dE_c/dr$  and  $dL_c^\xi/dr$ , and hence

$$\frac{dE_c}{dL_c^\xi} = \frac{1}{\xi r^2} \left( r^3 \Phi' \right)^{1-(\xi/2)}. \quad (\text{B2})$$

Combining Equations (B1) and (B2) we get

$$\Phi'(r) = \left( -\frac{\tilde{\beta}}{\gamma\xi} \right)^{2/(\xi-2)} r^{(2-3\xi)/(\xi-2)}. \quad (\text{B3})$$

Integrating, we have

$$\Phi(r) = \left( -\frac{\tilde{\beta}}{\gamma\xi} \right)^{2/(\xi-2)} \frac{(2-\xi)}{2\xi} r^{2\xi/(2-\xi)} + C, \quad (\text{B4})$$

and applying the Poisson equation finally gives Equation (2):

$$\rho(r) = \frac{1}{4\pi} \left( -\frac{\tilde{\beta}}{\gamma\xi} \right)^{2/(\xi-2)} \left( \frac{2+\xi}{2-\xi} \right) r^{-4(\xi-1)/(\xi-2)}. \quad (\text{B5})$$

Not all combinations of parameters  $\tilde{\beta}$ ,  $\gamma$ ,  $\xi$  are allowed. The factor  $[-\tilde{\beta}/(\gamma\xi)]^{2/(\xi-2)}$  in the above equations tells us that  $\tilde{\beta}/(\gamma\xi)$  has to be negative. There are four ways of realizing this, and we discuss these cases separately. In **Ia** and **Ib**, the inverse temperature is negative,  $\tilde{\beta} < 0$ , as in DARKexp, but in **IIa** and **IIb**, it is positive. Note that all four cases guarantee that  $dE_c/dL_c > 0$ , i.e. that as the energy of a circular orbit is increasing, its angular momentum must increase as well. On the other hand, Equation (B2) can have either sign.

**Case Ia:**  $\tilde{\beta} < 0$ ,  $\gamma > 0$  and  $\xi > 0$ .

In Equation (A1) the term  $\gamma L^\xi$  is independent of energy, so for  $\tilde{\beta}E \rightarrow \tilde{\beta}\Phi_0$ ,  $N(E, L^2)$  can get as small as  $-1$ , i.e. it can become negative. This is not allowed, and so this combination of parameters is ruled out.

**Case Ib:**  $\tilde{\beta} < 0$ ,  $\gamma < 0$  and  $\xi < 0$ .

$N(E, L^2)$  cannot become negative, so in general, such solutions are allowed. Looking at the factor  $(2+\xi)/(2-\xi)$  in Equation (B5) we see that only  $-2 < \xi < 0$  are allowed. The factor  $(2-\xi)/(2\xi)$  in Equation (B4) guarantees that the potential is negative, so constant  $C$  can be set to zero. The two limiting solutions are: as  $\xi \rightarrow 0$ ,  $\rho(r) \rightarrow r^{-2}$ , and as  $\xi \rightarrow -2$ ,  $\rho(r) \rightarrow r^{-3}$ .

**Case IIa:**  $\tilde{\beta} > 0$ ,  $\gamma < 0$  and  $\xi > 0$ .

$N(E, L^2)$  in Equation (A1) can become negative, especially when  $E \rightarrow 0$ , and  $-\gamma L^\xi$  cannot compensate for negative  $\tilde{\beta}\Phi_0$ . Therefore this combination of parameters is ruled out.

**Case IIb:**  $\tilde{\beta} > 0$ ,  $\gamma > 0$  and  $\xi < 0$ .

$N(E, L^2)$  is always negative, so this combination of parameters is not allowed.

We conclude that if  $L^\xi$  is treated the same way as total mass and total energy, then maximizing entropy subject to condition of Equation (B1) gives potential and density profiles that are power laws in radius, with the values of constants  $\tilde{\beta}$ ,  $\gamma$ ,  $\xi$  given by **Case Ib**, and the allowed density profile slopes spanning the range from  $-2$  to  $-3$ . Just like in Appendix A, we conclude that the solutions obtained here are very different from DARKexp, and very different from systems obtained in numerical simulations.

It is interesting to note that Equation (A1) does not reduce to DARKexp for isotropic systems. When  $\xi \rightarrow 0$ , Equation (A1) becomes  $N(E, L^2) \propto \exp(\tilde{\beta}\Phi_0 - \tilde{\beta}E - \gamma) - 1$ . Because  $\gamma$  cannot be 0 (see Equation B1), the  $N(E, L^2)$  distribution does not reduce to DARKexp for any allowed parameter values.

The Dark Cosmology Centre (DARK) is funded by the Danish National Research Foundation. L.L.R.W. would like to thank DARK for their hospitality. The authors are grateful to Stefan Gottlöber, who kindly allowed one of his CLUES simulations,

(<http://www.clues-project.org/simulations.html>) to be used in this paper. The simulation has been performed at the Leibniz Rechenzentrum (LRZ) Munich.

## REFERENCES

- An, J. H., & Evans, N. W. 2006, ApJ, 642, 752  
 Ascasibar, Y., Hoffman, Y., & Gottlöber, S. 2007, MNRAS, 376, 393  
 Beraldo e Silva, L. J., Lima, M., & Sodr e, L. 2013, ArXiv e-prints, 1301.1684  
 Binney, J., & Tremaine, S. 2008, Galactic Dynamics: Second Edition (Princeton University Press)  
 Biviano, A., & Poggianti, B. M. 2009, A&A, 501, 419  
 Biviano, A., et al. 2013, ArXiv e-prints, 1307.5867  
 Chavanis, P.-H. 1998, MNRAS, 300, 981  
 Ciotti, L., & Morganti, L. 2010, MNRAS, 408, 1070  
 Dalal, N., Lithwick, Y., & Kuhlen, M. 2010, ArXiv e-prints, 1010.2539  
 Hansen, S. H., & Sparre, M. 2012, ApJ, 756, 100  
 Hjorth, J. 1994, ApJ, 424, 106  
 Hjorth, J., & Madsen, J. 1991, MNRAS, 253, 703  
 Hjorth, J., & Williams, L. L. R. 2010, ApJ, 722, 851  
 Host, O., Hansen, S. H., Piffaretti, R., Morandi, A., Ettori, S., Kay, S. T., & Valdarnini, R. 2009, ApJ, 690, 358  
 King, I. R. 1966, AJ, 71, 64  
 Kuhlen, M., Weiner, N., Diemand, J., Madau, P., Moore, B., Potter, D., Stadel, J., & Zemp, M. 2010, JCAP, 2, 30  
 Lapi, A., & Cavaliere, A. 2009, ApJ, 692, 174  
 Le Delliou, M., & Henriksen, R. N. 2003, A&A, 408, 27  
 Lemze, D., et al. 2012, ApJ, 752, 141  
 Levin, Y., Pakter, R., & Rizzato, F. B. 2008, Phys. Rev. E, 78, 021130  
 Libeskind, N. I., Hoffman, Y., Forero-Romero, J., Gottlöber, S., Knebe, A., Steinmetz, M., & Klypin, A. 2013, MNRAS, 428, 2489  
 Lu, Y., Mo, H. J., Katz, N., & Weinberg, M. D. 2006, MNRAS, 368, 1931  
 Ludlow, A. D., Navarro, J. F., White, S. D. M., Boylan-Kolchin, M., Springel, V., Jenkins, A., & Frenk, C. S. 2011, MNRAS, 415, 3895  
 Lynden-Bell, D. 1967, MNRAS, 136, 101  
 Madsen, J. 1996, MNRAS, 280, 1089  
 Navarro, J. F., Frenk, C. S., & White, S. D. M. 1997, ApJ, 490, 493  
 Navarro, J. F., et al. 2004, MNRAS, 349, 1039

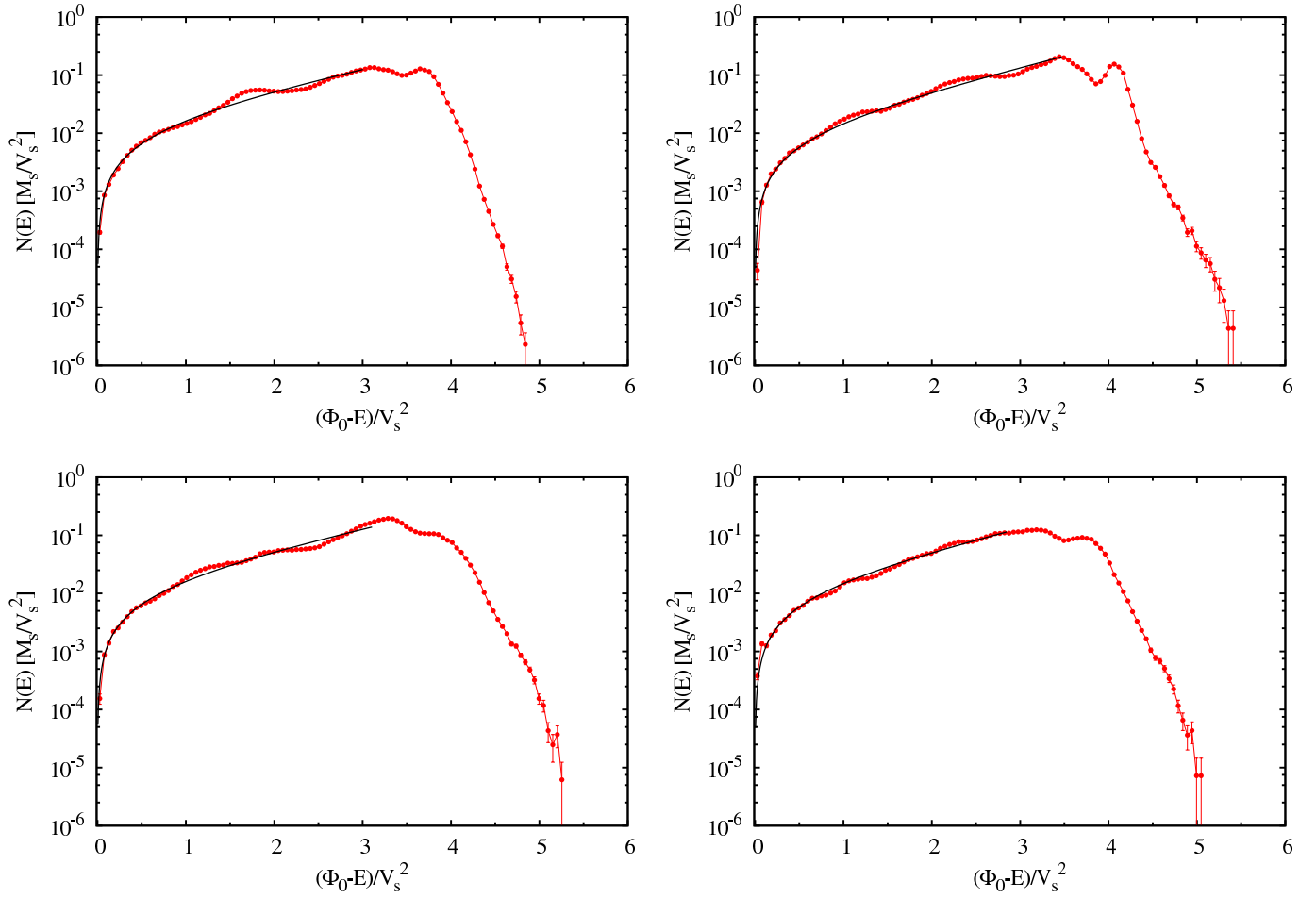


**Figure 1.** Comparison between  $N(E)$  of four randomly chosen halos from a cosmological  $N$ -body simulation (red curves with points and Poisson errorbars) and the DARKexp fits (black curves). The scalings on the axes are in terms of parameters ( $M$  is the enclosed mass,  $V$  is the circular velocity) measured at  $r_{-2}$ , which is the radius where the logarithmic density slope,  $d \ln \rho(r) / d \ln r$ , is equal to  $-2$ ; see Section 3.1 of Paper III for details.

—. 2010, MNRAS, 402, 21

Ogorodnikov, K. F. 1957, Soviet Ast., 1, 748

Pontzen, A., & Governato, F. 2013, MNRAS, 430, 121

Ryden, B. S., & Gunn, J. E. 1987, ApJ, 318, 15

Salvador-Solé, E., Manrique, A., González-Casado, G., & Hansen, S. H. 2007, ApJ, 666, 181

Spergel, D. N., & Hernquist, L. 1992, ApJ, 397, L75

Stadel, J., Potter, D., Moore, B., Diemand, J., Madau, P., Zemp, M., Kuhlen, M., & Quilis, V. 2009, MNRAS, 398, L21

Stiavelli, M., & Bertin, G. 1987, MNRAS, 229, 61

Williams, L. L. R., Babul, A., & Dalcanton, J. J. 2004, ApJ, 604, 18

Williams, L. L. R., Barnes, E. I., & Hjorth, J. 2012, MNRAS, 423, 3589

Williams, L. L. R., & Hjorth, J. 2010, ApJ, 722, 856

Williams, L. L. R., Hjorth, J., & Wojtak, R. 2010, ApJ, 725, 282

Wojtak, R., Gottlöber, S., & Klypin, A. 2013, MNRAS, 434, 1576

Wojtak, R., Lokas, E. L., Mamon, G. A., Gottlöber, S., Klypin, A., & Hoffman, Y. 2008, MNRAS, 388, 815



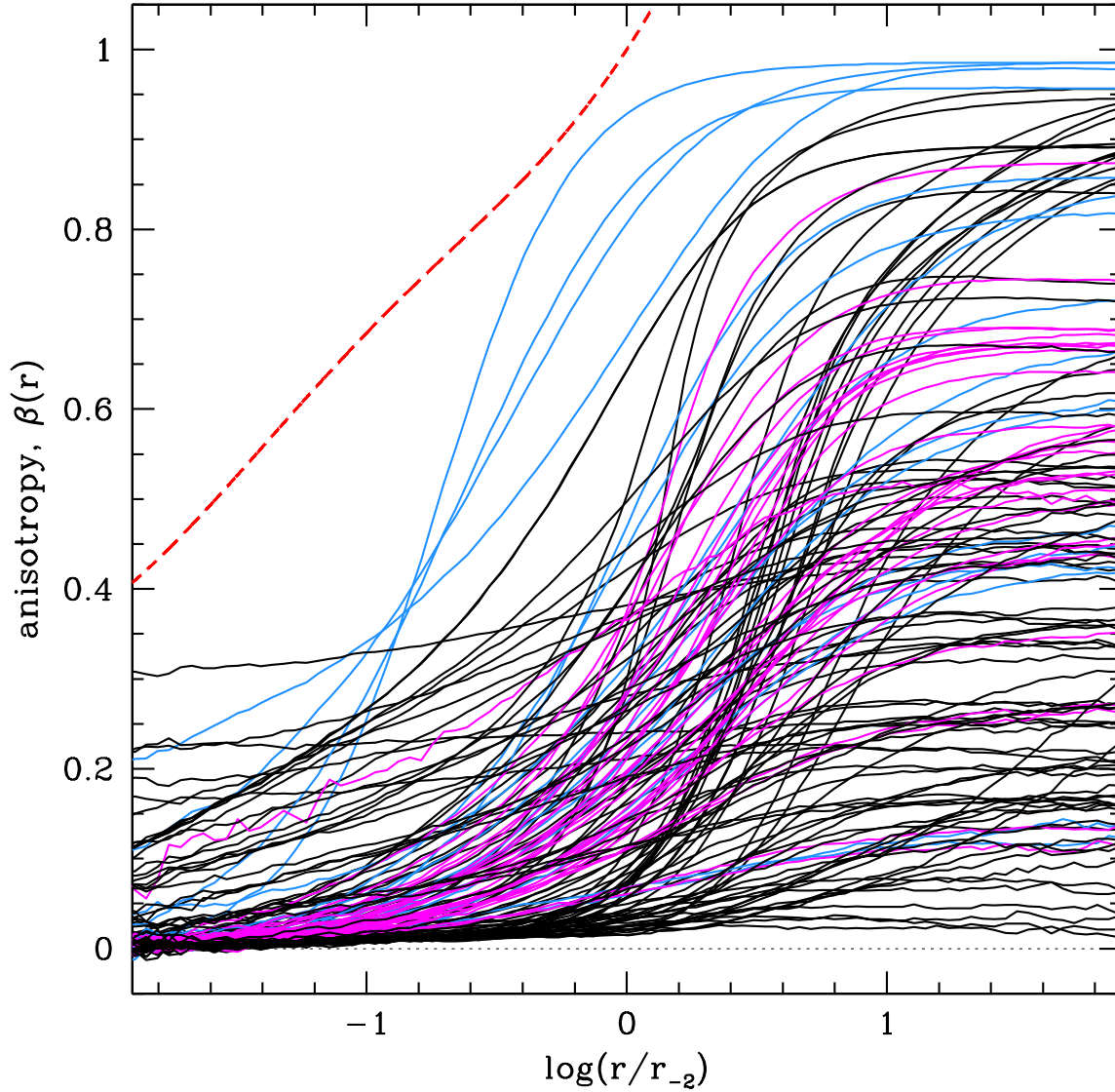


**Figure 2.** Anisotropy profiles for all the halos used in this paper. The red dashed curve corresponds to  $\frac{1}{2} [-d \ln \rho(r) / d \ln r]$  of DARKexp  $\phi_0 = 4$ , and represents the upper limit on the anisotropy derived by An & Evans (2006); Ciotti & Morganti (2010). We disallowed monotonically decreasing values of  $\beta(r)$ . Small fluctuations in  $\beta(r)$  are due to numerical noise. We highlight in color  $\beta(r)$  profiles from two prescriptions: Equation 4 and 5 are shown as magenta and blue curves, respectively.

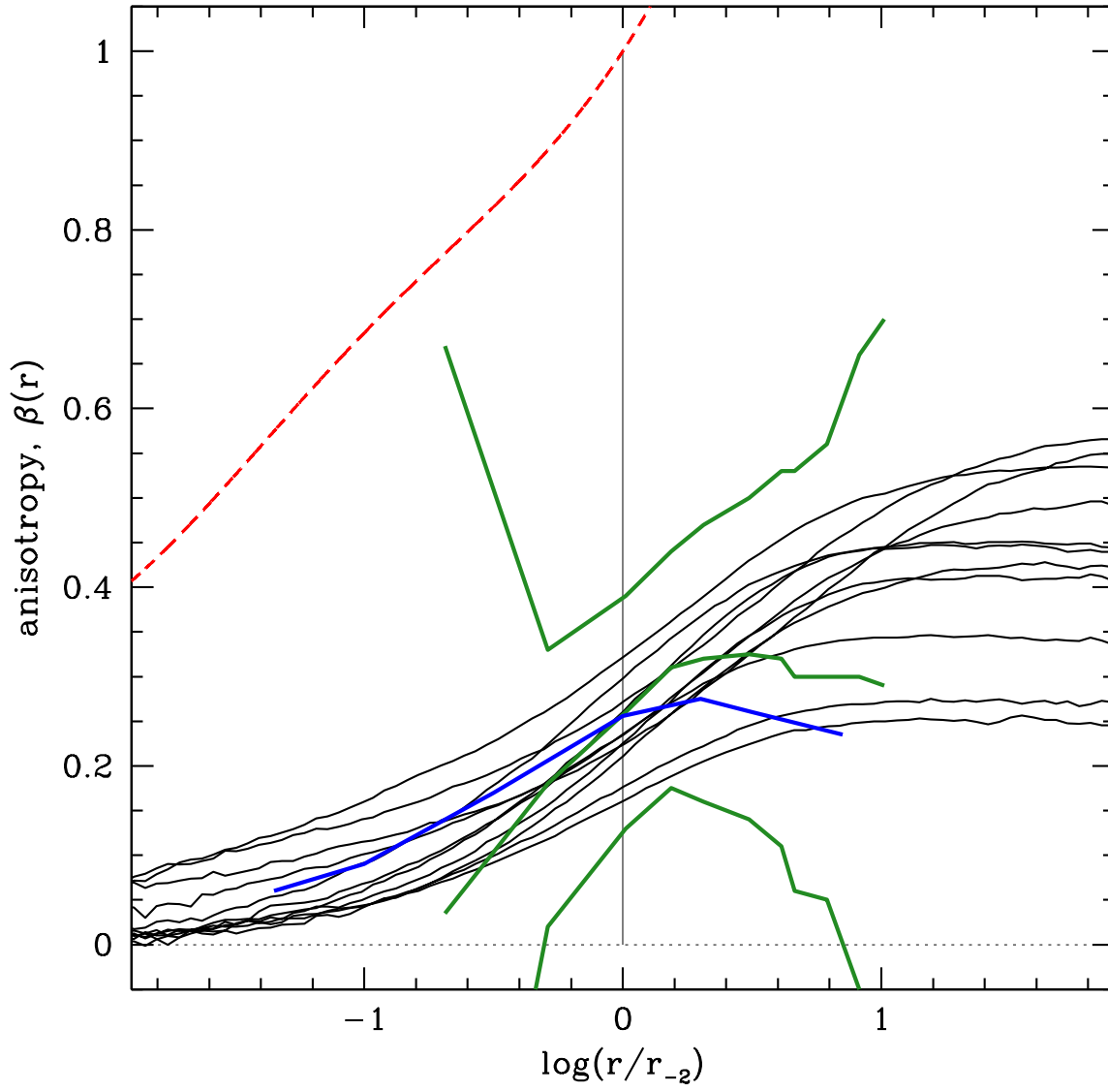


**Figure 3.** Similar to Fig. 2. Here we compare our anisotropy profiles (black curves) with those from numerical simulations. The blue curve is the average profile from Fig. 3b of Ludlow et al. (2011). The green curves are the average and upper and lower limits of relaxed systems taken from Lemze et al. (2012) (blue curves in their Fig. 13). Because their radius is in units of the virial radius while our systems do not have a defined virial radius, we scaled their horizontal axis to have the same velocity anisotropy value at  $r_{-2}$  as the Ludlow et al. (2011) data. A subset of our models that fit comfortably within the green curve bounds are shown in black.

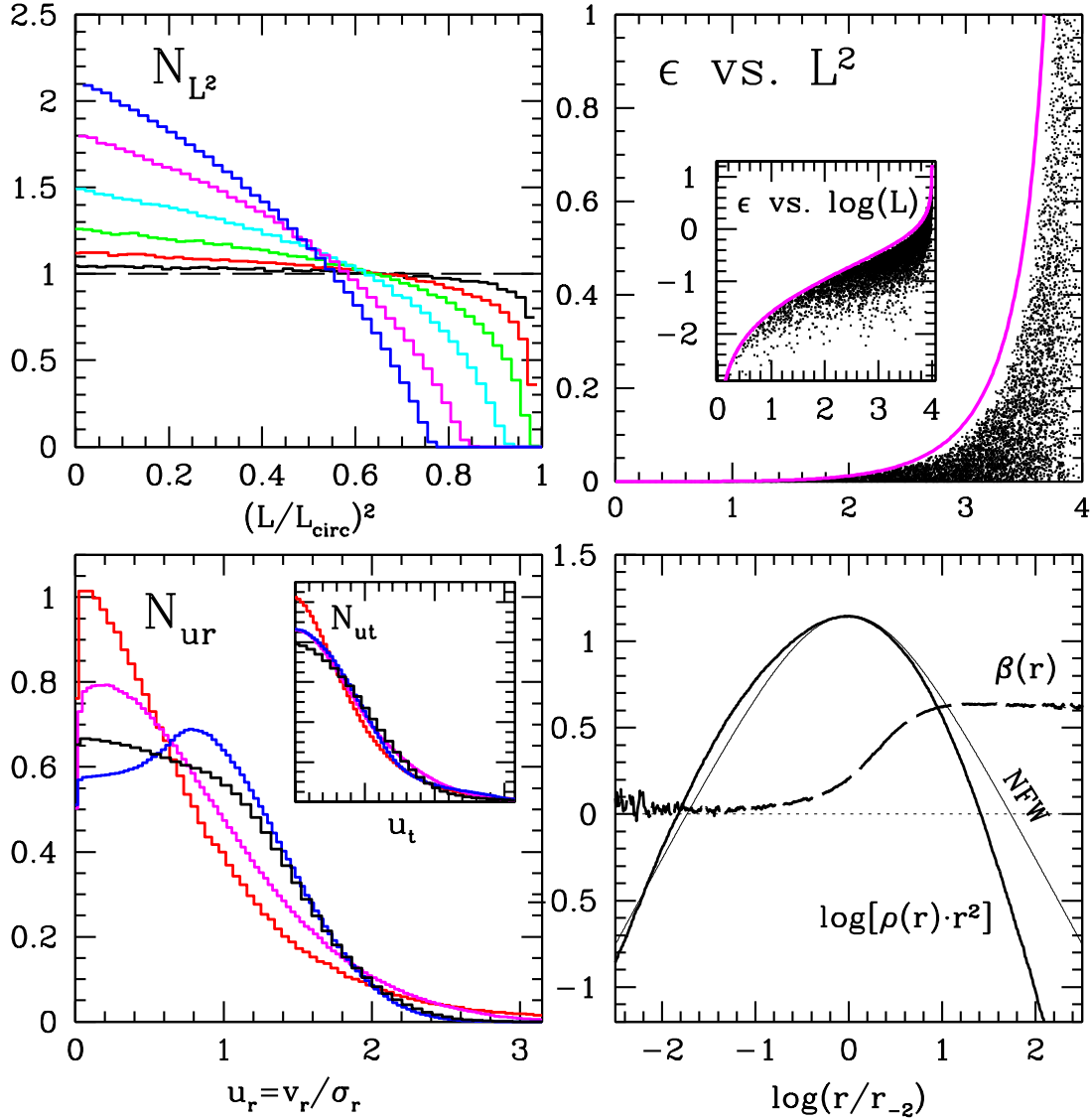


**Figure 4.** An example of a halo. The halo is DARKexp with  $\phi_0 = 4$ . (Vertical axis labels are shown inside the individual panels.) *Upper Left:* Each curve is the distribution of particles in  $\ell^2 = (L/L_{\text{circ}})^2$ , where  $L_{\text{circ}}$  is the maximum angular momentum at that energy. The orbits are divided into six bins, of equal  $\Delta\epsilon$ . In ascending order in energy (most to least bound particles), the six energy bins are black, red, green, cyan, magenta, and blue. *Upper Right:* The  $N(E, L^2)$  distribution. The upper magenta envelope corresponds to circular orbits,  $L_{\text{circ}}$ . The main plot shows  $L^2$  plotted linearly. The inset shows  $\log(L)$ . Only a few hundred points are plotted, whereas our halos have about  $10^7$  particles each. *Lower Left:* The radial (main plot) and tangential (inset) velocity distribution functions for four radial intervals in the halo: red (inner most), black (outer most). *Lower Right:* Log of density times  $r^2$ . (Normalization is arbitrary.) NFW profile is shown for comparison, as a thin solid line. Anisotropy profile for the DARKexp halo is shown as a dashed line. The horizontal axis is radius in units of  $r_{-2}$ , where density profile has an instantaneous log-log slope of  $-2$ .

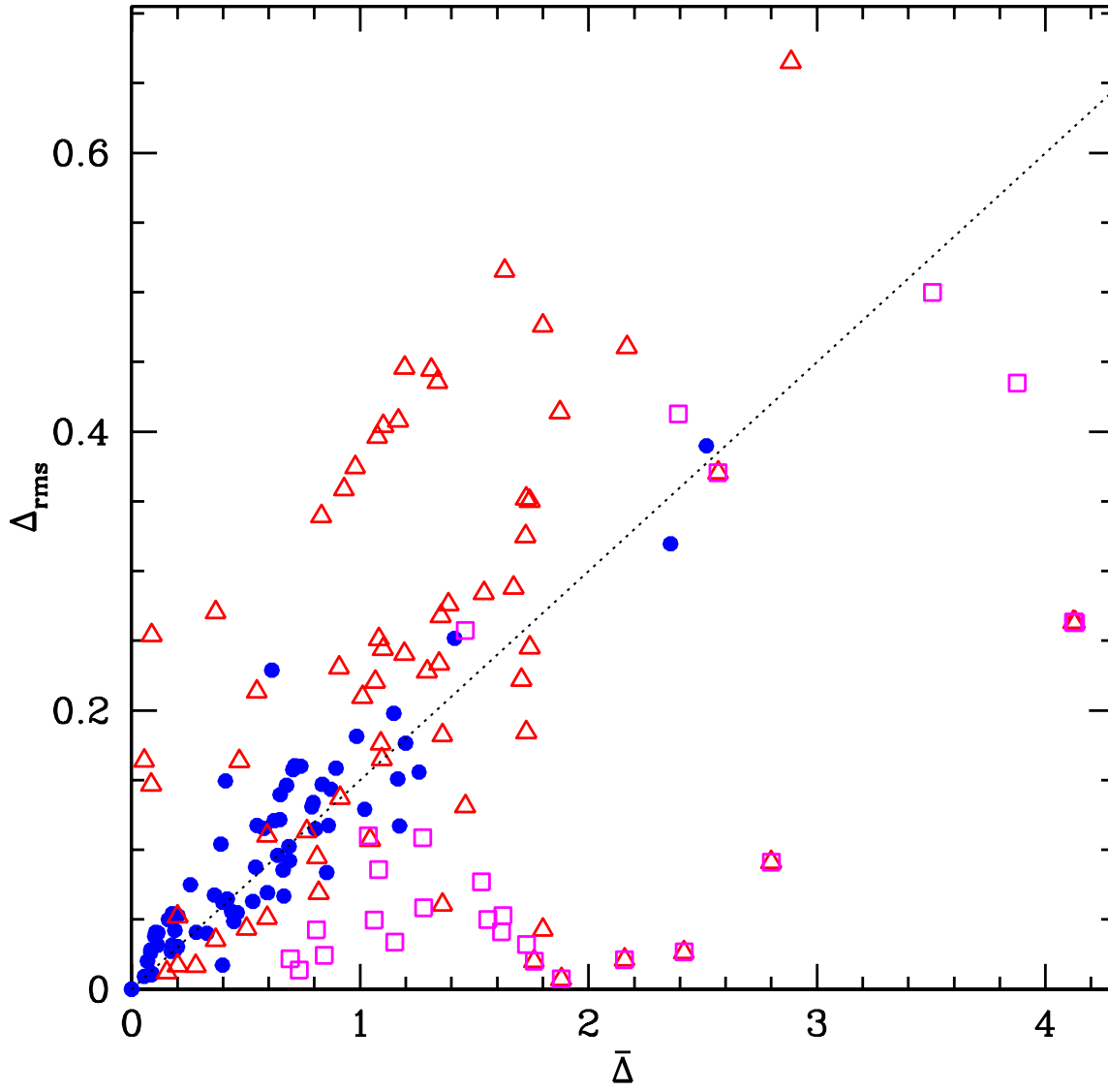


**Figure 5.**  $\bar{\Delta}$  vs.  $\Delta_{\text{rms}}$ , both of which are determined from  $N_{L2}$ . Red triangle points represent halos with VDF craters,  $\Upsilon > 0$ . Magenta squares represent halos with  $B > 0.1$ . Blue points gave  $B < 0.1$  and  $\Upsilon < 0$ . The diagonal line roughly separates the two. See Sections 3.2 and 3.3 for details.

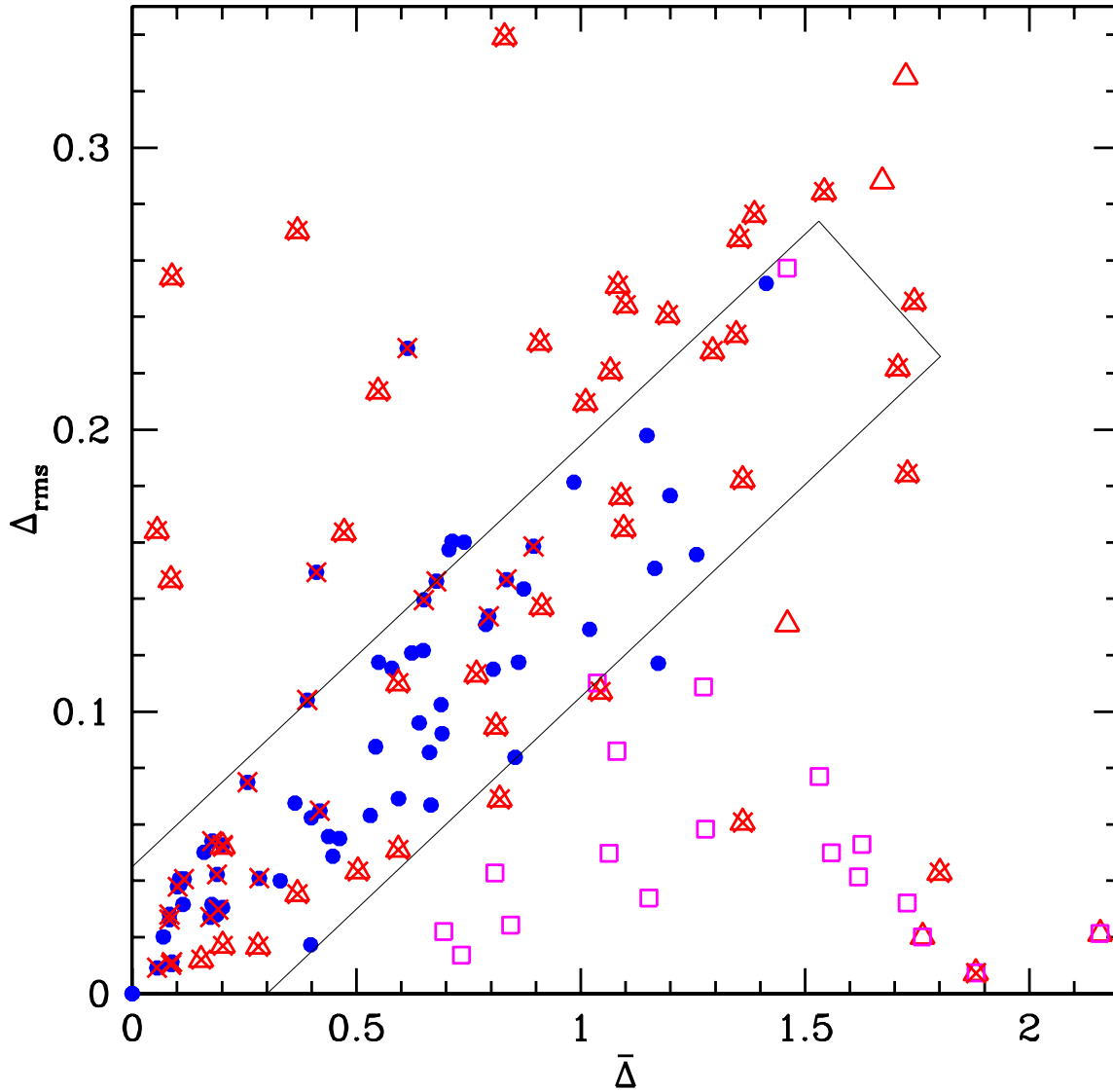


**Figure 6.** Zoom-in on Figure 5, now showing the systems with concave  $N_{L2}$  distributions ( $K > 0$ ) marked with red crosses. The upper limits on  $\bar{\Delta}$  and  $\Delta_{\text{rms}}$  do not extend as far as in Figure 5; this eliminates systems with  $\beta(r)$  near 1 at large radii. The diagonal rectangular box delineates our selection criteria. Systems that are inside the box and are not marked with a red cross have realistic VDF and  $\beta(r)$  profiles. See Sections 3.2 and 3.3 for details.

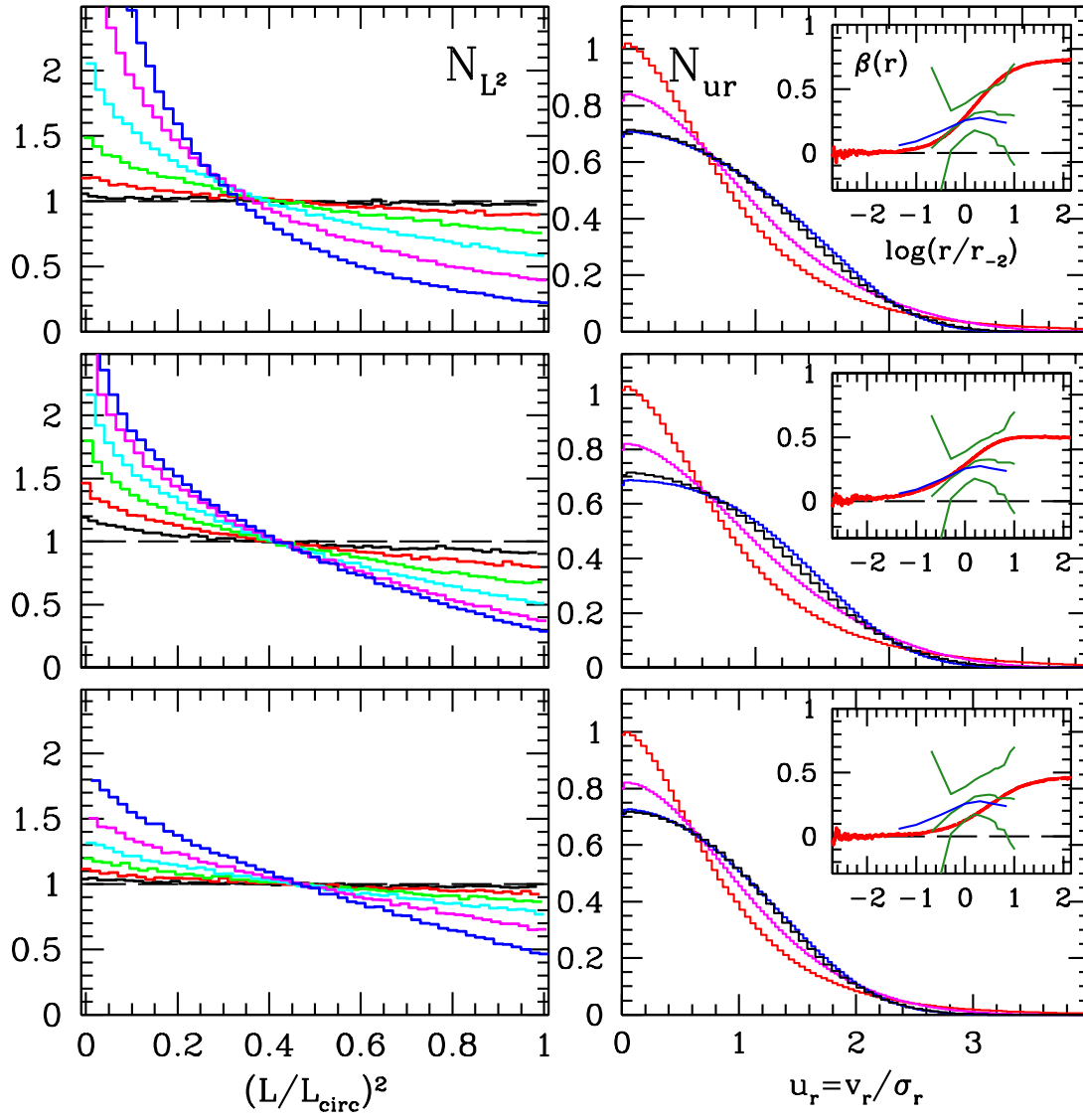


**Figure 7.** Examples of the angular momentum distribution, VDF, and anisotropy profiles of three realistic systems. The blue curve in the inset of the right panels is the average simulated velocity anisotropy profile from Fig. 3b of Ludlow et al. (2011). The green curves are the average and upper and lower limits of relaxed systems taken from Lemze et al. (2012). See the caption of Figure 3 for details.

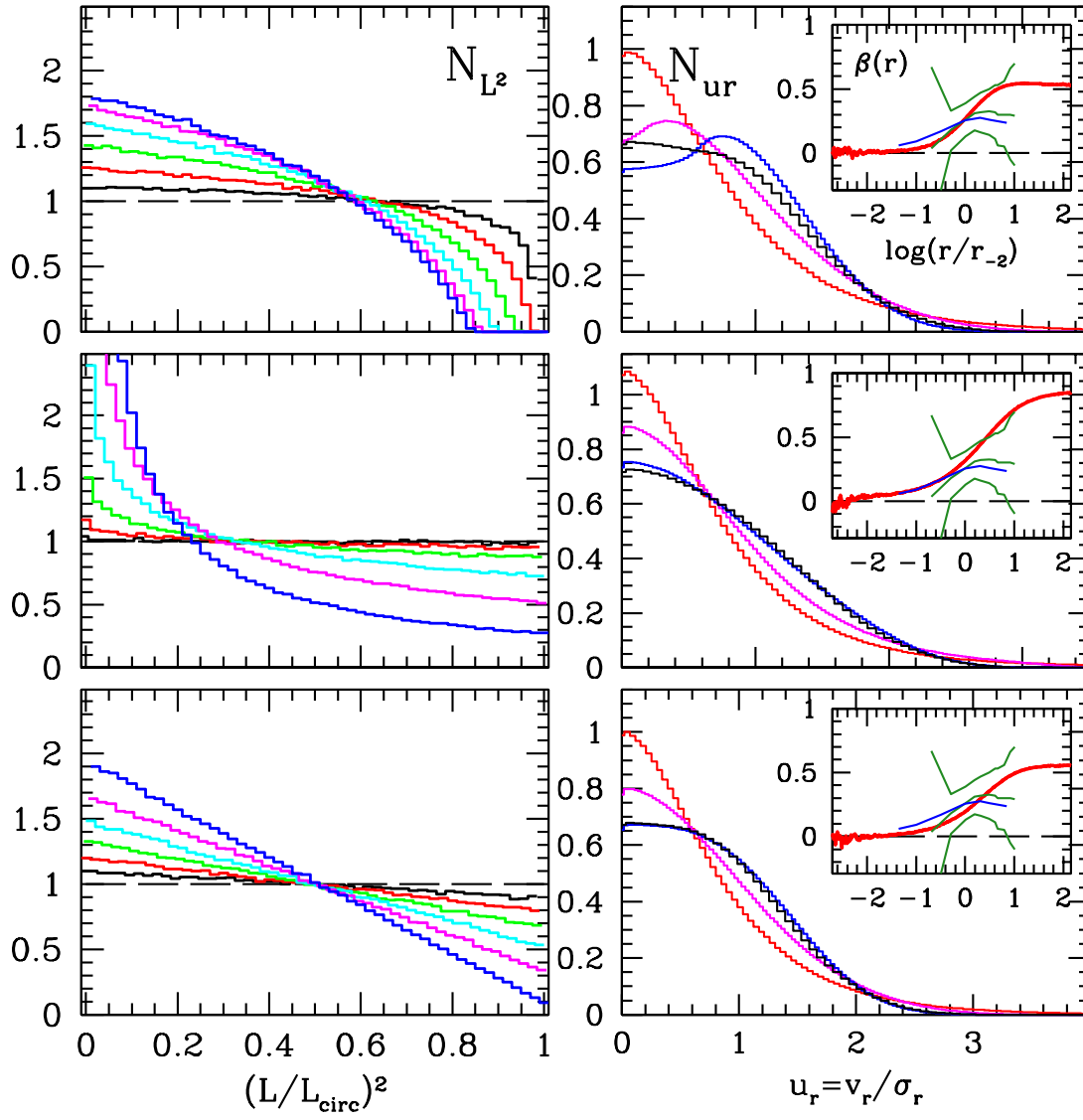


**Figure 8.** Similar to Figure 7 for 3 systems inside the rectangular box of Figure 6. The top row shows a system that was correctly eliminated as unrealistic by our criteria, and for the other two systems our criteria fail; see Section 3.3 for details.

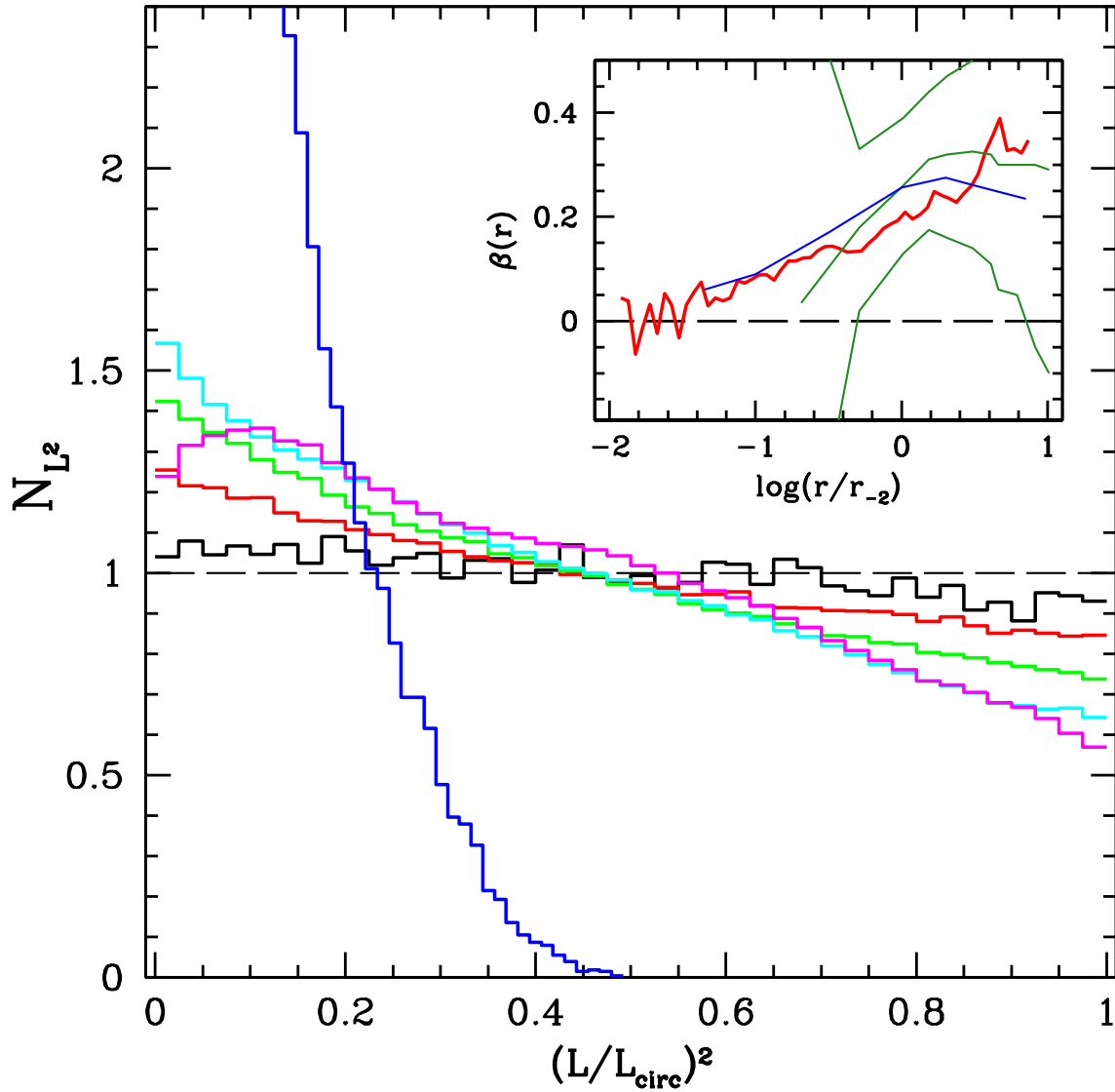


**Figure 9.** The  $(L/L_{\text{circ}})^2$  distribution from N-body simulations of cluster-sized halos, using the color scheme similar but identical to the one in other plots in this paper. The inset shows spherically averaged anisotropy profile. This is the same set of halos that were shown to follow DARKexp  $N(E)$  in Paper III. The blue curve in the inset of the right panel is the average simulated velocity anisotropy profile from Fig. 3b of Ludlow et al. (2011). The green curves are the average and upper and lower limits of relaxed systems taken from Lemze et al. (2012). See the caption of Figure 3 for details.



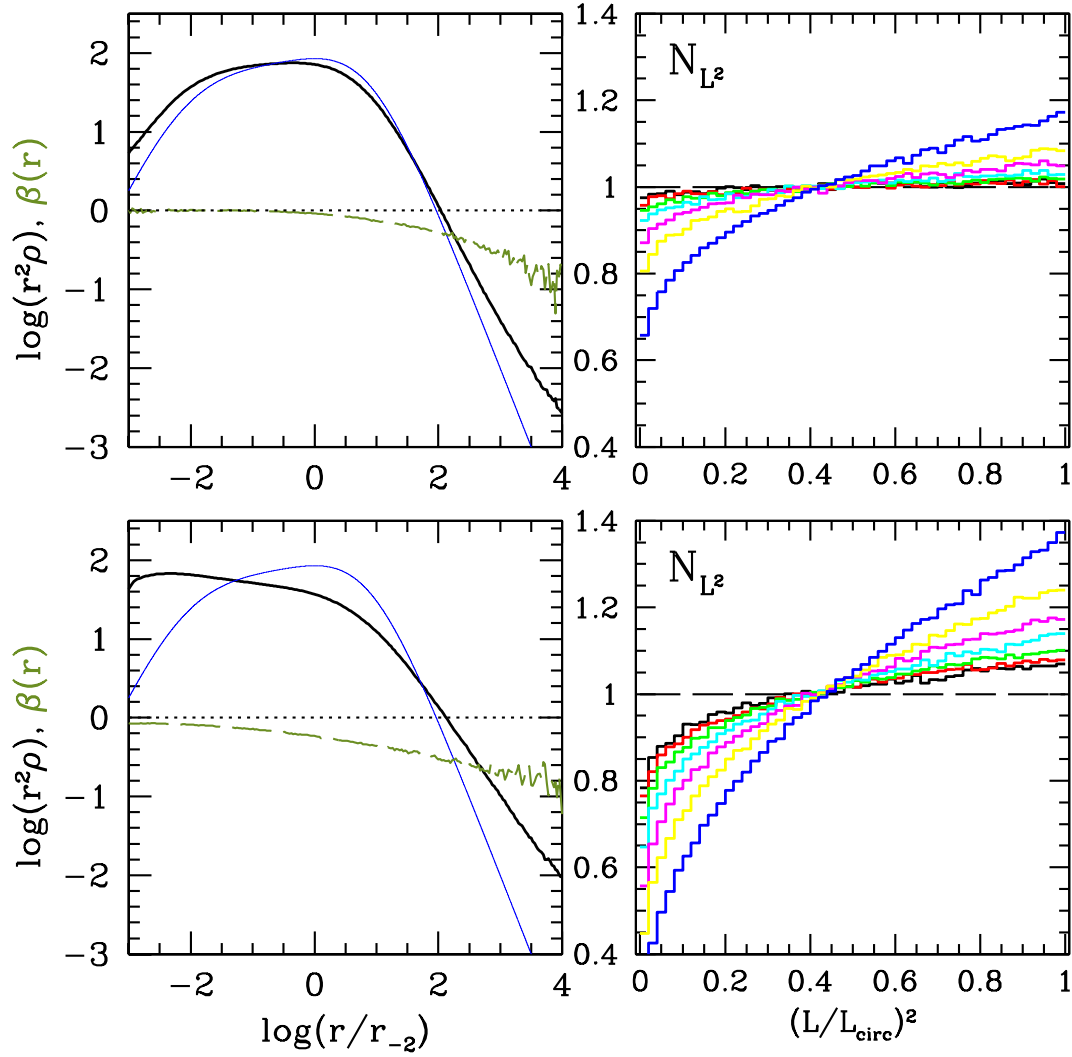


**Figure 10.** Examples of two systems obeying Equation 1, with  $\gamma = -1$ ,  $\xi = 0.5$ ,  $\phi_0 = 6$  (top panels) and  $\gamma = -5$ ,  $\xi = 0.2$ ,  $\phi_0 = 6$  (bottom panels). The density profiles are multiplied by  $r^2$  and plotted in the left panels as thick black curves; the blue thin lines are DARKexp with  $\phi_0 = 6$  shown for comparison. The horizontal axis is in units of  $r_{-2}$  of the corresponding DARKexp profile. Right panels present the distribution of  $L^2$ , which is to be compared to those in Figure 7. The distributions of  $L^2$  in the present figure are biased towards high angular momenta, which is also reflected in the anisotropy profile (olive-green long-dash line in left panels).